Hydrogen Diffusivity and Trapping in Custom 465 Stainless Steel

S. Ifergane,[1,2] R. Ben David,[3] E. Sabatani,[2] B. Carmeli,[2] O. Beeri,[2] and N. Eliaz [1,*,z]

[1]*Department of Materials Science and Engineering, Tel-Aviv University, Ramat Aviv, Tel Aviv 6997801, Israel*
[2]*Nuclear Research Center Negev, Beer Sheva 84190, Israel*
[3]*Israel Atomic Energy Commission, Tel Aviv, Israel*

Custom 465 is an advanced precipitation hardened martensitic stainless steel exhibiting a combination of high strength, high fracture toughness and good corrosion resistance. This steel is recommended for use in hydrogen atmospheres, yet only little research has been published on hydrogen behavior in this alloy. Here, the diffusivity, solubility and average detrapping energy for hydrogen were compared in various thermal conditions (solution annealed, H900 and H1000), employing electrochemical permeation and thermal programmed desorption measurements. It is suggested that reversible (low energy) traps in the H900 and H1000 conditions, associated with (semi)coherent η-Ni_3Ti precipitates, are responsible for the high hydrogen solubility and low diffusivity. At the peak of coherency of the precipitates in the H900 condition, higher solubility and lower diffusivity and detrapping energy were measured. The value of the diffusion coefficient is found to change during different stages of charging and discharging, depending on the level of occupancy of the reversible traps.

 [DOI: 10.1149/2.0261803jes]

Manuscript submitted December 19, 2017; revised manuscript received January 29, 2018. Published February 13, 2018.

Carpenter Technology's Custom 465 (UNS S46500) is an advanced precipitation hardened (PH) martensitic stainless steel, characterized by a combination of high strength and fracture toughness with good corrosion resistance, compared to other PH stainless steels.[1–3] Although this steel is recommended for engineering applications in corrosive environments that contain hydrogen, only little work has been published on hydrogen interaction with this steel, to the best of our knowledge.[4–6] Hydrogen diffusivity is affected by the microstructure that results from different thermal treatments.[4] The microstructure of Custom 465 steel[7] in the solution annealed (SA) condition consists of Fe-Ni martensite, which is characterized by blocks of parallel lamellae organized in packets along the prior austenite grains. During aging, η-Ni_3Ti nano-precipitates are formed inside the lamella, and reverted austenite at grain boundaries and interlamella boundaries. For engineering applications, both H900 and H1000 age conditions are mostly recommended.[1] In the H900 (482°C/ 4 hours) age condition,[7] the (semi)coherent rod-shape nanoprecipitates of η-Ni_3Ti, about 3 nm in diameter and 8 nm long, are formed, and a maximal ultimate tensile strength (UTS) of about 260 ksi (1793 MPa) is obtained. In the H1000 (540°C/ 4 hours) age condition, precipitates grow to about 9 nm in diameter and 27 nm in length. Due to the lower coherency of the precipitates and their lower density in the H1000 condition, the UTS decreases to 225 ksi (1551 MPa). At the same time, the ductility, fracture toughness, general corrosion and stress corrosion cracking (SCC) resistance all improve.[1] In both the H900 and H1000 age conditions, the reverted austenite concentration is less than 5 vol.%, and it is dispersed as discrete particles.[7]

The fundamental correlation between the microstructure change during aging and hydrogen behavior in PH martensitic stainless steels has been studied to limited extent. For example, the effect of aging temperature on hydrogen diffusivity in PH 13-8Mo was reported.[8,9] The effect of aging temperatures on the detrapping energies and solubility in PH martensitic stainless steel has not been reported yet, to the best of our knowledge. Here, the effects of heat-treatment on hydrogen diffusivity, solubility, permeability and the average detrapping energies in the H900 and H1000 age conditions as well as in the SA condition are reported. To this aim, electrochemical hydrogen permeation (EP) and thermal programmed desorption (TPD) tests were employed. The effect of hydrogen trapping on its diffusivity and its origin in the different age conditions is discussed. The microstructure changes reported in our previous work[7] are correlated with hydrogen behavior in different thermal conditions.

Experimental

Specimen preparation.—Custom 465 stainless steel in the form of 2-inch diameter rod was purchased from Carpenter Technology (Wyomissing, PA, USA). The composition of this steel (wt%) was determined by Inductively Coupled Plasma Atomic Emission Spectroscopy (ICP-AES) as Fe–10.7Cr–10.9Ni–0.86Mo–1.4Ti–0.04Al–0.04Zn–0.0046C. The rod was received in the SA and cold-treated condition.[1,7] Three specimen types were tested in the transverse direction: (1) ***SA*** : solution annealed condition, (2) ***H900*** : aged at 482°C, and (3) ***H1000*** : aged at 540°C. Aging was performed in an argon shielding atmosphere for 4 h, by the same procedure as in Ref. 7, in order to enable comparison between the results. Subsequently, cooling in the same atmosphere was done. The heating and cooling rates were 10°C/min and 40–60°C/min, respectively. After aging, all specimens were ground on both sides on a 1000 grit SiC grinding paper and polished with 6 μm and 1 μm diamond pastes.

Electrochemical hydrogen permeation (EP).—The EP tests were carried out in a two-compartment cell, originally developed by Devanathan and Stachurski,[10–12] with the 0.12–0.2 mm thick specimen being a membrane separating between the two compartments, as described in Ref. 4. System validation was conducted with Pd–0.1 wt%Pt specimens. In the final preparation step prior to the onset of the permeation test, the surface oxide film was removed by grinding on a SiC paper FEPA P4000 (particle size 5 μm). Afterwards, the specimens were rinsed in detergent, washed in water, ultrasonically cleaned in acetone, dried quickly in high-pressure air, washed in ethanol, and dried under high-pressure room-temperature air. Following surface activation in a 2 N HF + 2.5 N HNO_3 aqueous solution for 10 s and water rinse, the specimens were electrochemically coated with a thin layer of palladium (thickness 4 ± 1 nm). The Pd thickness was determined based on the charge passed during electrochemical stripping in 0.1 M H_2SO_4 + 0.02 M KCl solution. During hydrogen charging, the hydrogen entry (cathodic) side was galvanostatically polarized by a negative current density of 1.3 mA/cm^2 in 0.05 M NaOH solution, using an Altek model 234 current supplier and a 0–20 mA signal analyzer. Simultaneously, the hydrogen exit (anodic) side was maintained at a constant potential of 100 mV versus a Hg/HgO/0.1 M KOH reference electrode (–70 mV vs. SCE), and the resulting anodic current was recorded using an Autolab PGstat 30 potentiostat/galvanostat. Note that this reference electrode is recommended for use in alkaline solutions (as in this study) and eliminates the risk of leakage of impurities such as chlorides from the reference electrode to the electrolyte solutions. When connecting a current supplier and a potentiostat to the same membrane, they were electrically floating. Since two

*Electrochemical Society Member.
zE-mail: neliaz@tau.ac.il

electric double layers are formed, one on each side of the membrane, the electrochemical potential on the two sides of the membrane can be different. During decay (discharge), a positive potential of +100 mV vs. Hg/HgO/0.1M KOH was applied on the entry side, using a DATEL DVC 350A voltage supplier, in order to set the zero concentration boundary condition for hydrogen diffusion at the entry side. In this case too, the hydrogen exit side was held at a constant potential of 100 mV vs. Hg/HgO/0.1 M KOH, and the resulting anodic current was recorded using an Autolab PGstat 30 potensiostat/galvanostat.

The measured anodic current is a direct indication of hydrogen flow rate out of the specimen. During charging, the current rises until a steady-state is reached, whereas during discharge the current decays until the background level is obtained. For each specimen, the experiment was performed until consecutive charging-decay cycles exhibited repeatable rise and decay transients. All tests were performed at room temperature. Argon gas was purged for at least 30 min prior to cathodic polarization and during the entire experiment, to remove oxygen. The cathodic side was polarized only after the background oxidation currents measured at the anodic side were lower than 0.1 $\mu A/cm^2$.

The EP tests allowed for determination of hydrogen diffusivity, permeability and subsurface concentration, and provided valuable information on the effect of reversible and irreversible traps in this steel. Variations in the steady-state current density were obtained due to small perturbations in the charging conditions (cathodic current density, gas purging, temperature, impurities in solution, pH, surface condition, etc.), as reported by Turnbull.[13] Nevertheless, while the measured permeation and hydrogen subsurface concentration values might be affected by this variation, the diffusion coefficient is not.

Temperature programmed desorption (TPD).—Hydrogen TPD measurements were performed using a home-made TPD apparatus coupled with a quadrupole mass spectrometer (QMS) detector and a supersonic molecular beam (SMB) inlet. Detailed description of the TPD-MS-SMB system is given elsewhere.[14] TPD measurements were carried out at heating rates of 5, 10, 15, and 20 °C/min, from room temperature to 600°C, under He (99.999%) flow conditions with a flow rate of 50 mL/min. Specimen charging and preparation for TPD measurements were done as follows: before hydrogen charging, 50 mm long and 12 mm wide rectangular pieces were ground down to a thickness in the range of 0.240–0.260 mm, and finally polished to 1 μm. In the final preparation step prior to the onset of hydrogen charging, the surface oxide film was removed by grinding with a SiC paper FEPA P4000 (particle size 5 μm). Cleaning of the specimens was done following the same procedure described above for the EP tests. Hydrogen charging was performed in 0.05 M NaOH solution, at a negative current density of 9 mA/cm^2 for 14 days at room temperature. At the end of charging, specimens were rinsed in Millipore distilled water, dried by pressurized air, inserted within maximum 30 seconds to liquid nitrogen, and kept in it for up to 5 hours before inserting to the TPD reactor. For a single TPD measurement, several pieces were cut from the specimens and inserted after drying into the specimen holders of the machine, so that the total mass of the pieces was kept within the range of 300 to 340 mg.

Analyses of the Diffusion Coefficients from EP Transients

This section describes the procedure used for computing the diffusion coefficient of hydrogen in the presence of high trap density. It is well recognized that high concentration of reversible traps hinders the diffusion process across the membrane significantly compared to diffusion in pure iron. Irreversible traps will always act as sinks for hydrogen, but reversible traps will play a mixed role (sink and source) since, by definition, they can take or give hydrogen.[15] The following analyses treat the case of repeatable cycles of the EP test, where the irreversible traps are full and the reversible traps are refilled during the charging-decay cycles. In this case, diffusion is a combination of reversible trapping and lattice diffusion.

This idea of extending Fick's first law to describe the diffusion problem is the basis of the seminal kinetic model introduced by McNabb and Foster:[16]

$$\frac{\partial C}{\partial t} + N\frac{\partial \theta}{\partial t} = D_{\mathrm{Fe}}\frac{\partial^2 C}{\partial x^2} \quad [1]$$

$$\frac{\partial \theta}{\partial t} = k_{\mathrm{abs}} C\,(1-\theta) - k_{\mathrm{des}}\theta \quad [2]$$

where C is the concentration of hydrogen in the interstitial sites, t is the time from beginning of charging/decay, N is the density of reversible trap sites, θ is the fractional occupancy of the reversible trap sites, D_{Fe} is the lattice diffusion coefficient of atomic hydrogen in iron, x is the diffusion coordinate, k_{abs} is the 2nd-order rate constant of hydrogen trapping, and k_{des} is the 1st-order rate constant of hydrogen escape out of the trap (detrapping).

McNabb-Foster equations cannot be solved analytically because of the intrinsic non-linear nature of the trapping process. For the same reason, it is clear that McNabb-Foster equations do not describe a simple diffusion process. The effective diffusion should be determined at different stages of the charging and decay processes, and not by a single diffusion coefficient along the whole decay process. The last idea is the motivation for the model discussed here. Oriani 1970[17] managed to derive an expression for the effective diffusivity when the occupancy of traps is low, i.e. $\theta \cong 0$. In this situation, the occupancy rate is low, $\dot{\theta} \cong 0$. Applying these assumptions to Eqs. 1 and 2, a simple expression was derived for the effective diffusion coefficient:

$$D_{\mathrm{eff}} = \frac{D_{\mathrm{Fe}}}{1 + N\frac{k_{\mathrm{abs}}}{k_{\mathrm{des}}}} \quad [3]$$

Eq. 3 is valid for a situation of low trap occupancy θ that prevails in the initial stages of charging and in the final stages of the decay transient. Under these conditions, very little hydrogen is still in the lattice, and most of the reversible traps are empty. At any other part of the transients, θ is not sufficiently small, even when $\dot{\theta} \cong 0$.

In contrast, in the late stage of charging and early stage of the decay transients, the occupancy of the reversible traps is at its maximum. Thus, the lattice hydrogen atoms are moving across the membrane with the smallest possible perturbation by traps, until they exit the membrane or reach an empty trap close to its exit side. Thus, it is expected that in these stages of the process, the effective diffusivity is higher compared to the effective diffusivity at low hydrogen occupancy, i.e.

$$D^{\mathrm{h}}_{\mathrm{eff}} > D^{\mathrm{l}}_{\mathrm{eff}} \quad [4]$$

where $D^{\mathrm{h}}_{\mathrm{eff}}$ and $D^{\mathrm{l}}_{\mathrm{eff}}$ are the effective diffusion coefficients measured at ***high*** and ***low*** occupancies of hydrogen in the lattice, respectively. Fitting the current curve at various stages of the charging and decay transients, as described below, can provide more information about diffusion and trapping.

The charging transient.—The boundary condition on the exit side ($x = L$, where L is the sheet thickness) is zero concentration during the entire experiment due to the positive potential imposed on the specimen, as defined by Eq. 5:

$$C\,(t, L) = 0 \quad [5]$$

To verify the applicability of Fick's second law to the permeation transient, the permeation transient is plotted in the form of normalized flux, $J(t)/J_{\mathrm{ss}}$, against the logarithm of the normalized time τ. The normalized transient is then compared with that derived from Fick's second law for rising transients:

$$\frac{J(t)}{J_{\mathrm{ss}}} = \frac{2L}{\sqrt{\pi Dt}}\sum_{n=0}^{\infty}\exp\left[-\frac{(2n+1)^2 L^2}{4Dt}\right] \quad [6]$$

A summation from $n = 1$ to 6 is sufficiently accurate according to ISO 17081 and ASTM G148; in many cases $n = 3$ is acceptable.[11] τ

Table I. Dimensionless inverted times $M=\tau^{-1}$ obtained for different normalized current density values according to Eq. 8.

Charging	$10\%j_{ss}$	$50\%j_{ss}$	$63\%j_{ss}$
Decay	$90\%j_{ss}$	$50\%j_{ss}$	$37\%j_{ss}$
$M=\tau^{-1}$	15.1	7.8	5.9

is the dimensionless time:

$$\tau = \frac{D_{\text{eff}} t}{L^2} \quad [7]$$

where t is the time from the beginning of the charging/decay transient. The effective diffusion coefficient D_{eff} for various stages of the charging transient is described by $D_{c\_X\%j_{ss}}$ for times $t_{c\_X\%j_{ss}}$ where X = 10%, 50%, and 63% is the ratio between the momentary current density and the final steady-state current density value, j_{ss}, expressed in terms of percentage. The D_{eff} for various stages on the charging transient were calculated from Eq. 7 by substituting the current density j according to the charging transient, when it reached 10%, 50%, and 63% of j_{ss}, into Eq. 8:

$$D_{c\_X\%j_{ss}} = \frac{L^2}{M \cdot t_{c\_X\%j_{ss}}} \quad [8]$$

The dimensionless times τ and their reciprocal values $M = \tau^{-1}$ for different normalized current values were calculated using Eq. 8. The results are given in Table I.

The decay transient.—The diffusion coefficients at different stages of the decay transient, $D_{d\_X\%j_{ss}}$, can be determined according to Eq. 8 and Table I, for times $t_{d\_X\%j_{ss}}$ on the decay transient where the current density decreases to X% of the initial steady-state current density value. Here, X = 90%, 50% or 37% of the decay transient. Further analysis enables fitting the experimental results according to the analytical solution of the effective diffusion equation. When steady state is obtained during charging, the hydrogen concentration distribution across the specimen is linear, as described by Eq. 9. This is the initial condition for the decay transient.

$$C(x) = C_0\left(1 - {}^{x}/_{L}\right) \quad [9]$$

where C_0 is the subsurface concentration of hydrogen at the entry side. The boundary condition at the exit side of the membrane is also common for all transient stages, with hydrogen concentration being equal to zero during the entire experiment (Eq. 5).

For the boundary condition on the entry side of the membrane, Eq. 10, we assume that the concentration is dropping to zero during the entire decay transient, since a positive potential was applied during this stage:

$$C(t, 0) = 0 \quad [10]$$

The flux versus time evolution in this case is according to the following solution of the diffusion equation:

$$\frac{j(t)}{j_{ss}} = \begin{cases} 1 - \frac{2L}{\sqrt{\pi D^{h}_{\text{eff}} t}} \sum_{n=0} e^{-\left(n+\frac{1}{2}\right)^2 \frac{L^2}{D^{l}_{\text{eff}} t}} \\ -\frac{2D^{l}_{\text{eff}}}{\pi D^{h}_{\text{eff}}} \sum_{n=1} (-1)^n e^{-n^2\pi^2 \frac{D^{l}_{\text{eff}} t}{L^2}} \end{cases} \quad [11]$$

The upper branch of Eq. 11, the LaPlace expression, is most suitable for an early time approximation because this expression rapidly decays when $t \to 0$. The upper branch of Eq. 11 was thus fitted to the experimental results for times in the initial stages of the decay transient and down to 90% of the steady-state current density, in order to obtain $D_{high\_90\%j_{ss}}$ for ***high*** trap occupancy. The lower branch of Eq. 11, the Fourier expression, was fitted to the final stages of the decay transient in the range where the current density dropped to 20–10% j_{ss}, in order to obtain $D_{low\_20-10\%j_{ss}}$ for ***low*** trap occupancy. $D_{high\_90\%j_{ss}}$ best represents the lattice diffusion, hence, integrating the upper branch of Eq. 11 (marked by D in Figs. 1b, 1d, 1f) represents the concentration of lattice diffusion-controlled hydrogen, as suggested by Zakroczymski.[18] The trapped hydrogen concentration (marked by T in Figs. 1b, 1d, 1f) is calculated by subtracting the concentration of lattice diffusion-controlled hydrogen from the total concentration of desorbed hydrogen, as determined by the integration of the experimental decay transient. The ratio between the trapped hydrogen concentration T and the total concentration of desorbed hydrogen for each specimen type is listed in Table II.

Results

Hydrogen permeation and the effect of reversible traps.—Charging and decay time transients of the permeation current density are shown in Fig. 1. For each specimen, analysis was performed from the 3rd cycle of each experiment, where the irreversible trap sites are assumed to be already at the maximal occupancy, and the charging and decay transients are repetitive. The analyses of these repetitive cycles are limited mostly to the reversible trap sites and lattice hydrogen. The diffusion coefficient was calculated at various stages of charging and decay cycles, as listed in Table I. For the three specimen types, the lattice diffusion coefficient $D_{high\_90\%j_{ss}}$, associated with the highest reversible trap occupancy, was higher by about half an order of magnitude compared to the diffusion coefficient at low trap occupancy, $D_{c\_10\%j_{ss}}$ and $D_{d\_10-20\%j_{ss}}$. The intermediate diffusion coefficients during charging ($D_{c\_50\%j_{ss}}$ and $D_{c\_63\%j_{ss}}$) and during decay ($D_{d\_50\%j_{ss}}$ and $D_{d\_37\%j_{ss}}$) fall well inside the range according to trap occupancy state. The diffusion coefficient in the final stage of charging is difficult to determine, as it is hard to point at the exact moment when charging ends and a steady state is attained. As mentioned above, in the initial stages of the decay transient, all of the reversible traps are filled, enabling faster hydrogen diffusion through the membrane. In contrast, in the final stages of the decay transient, almost all of the reversible traps are empty, and hydrogen diffusion is hindered by trapping. Thus, fitting of different values of diffusion coefficient was made both in the initial and in the final stages of the transients. Trapping and diffusion in the presence of reversible traps is illustrated schematiclly in Fig. 2. When the reversible traps are full, the activation energy for hydrogen diffusion becomes lower.

Figures 1g, 1h shows the relative position of the steep rise of the charging and the slow decay transients in the normalized current density (j/j_{ss}) versus log of the dimensionless time curves (Eqs. 6, 7). The diffusion coefficients in the age H900 and H1000 conditions are lower by a factor of 4 to 6 compared to that in the SA condition (see the data for H900 in Ref. 4), regardless of whether the charging or decay transient is analyzed. This finding is in accordance with data reported for other PH martensitic stainless steels,[8,9] see Table II.

In general, the diffusion coefficients measured in the H1000 and H900 conditions are similar. However, some variation exists between different regions of the transient. Firstly, a slower rise in the initial part of the charging transient, followed by steep rise, is evident for H900 compared to H1000. It seems that the diffusion coefficient related to the charging transient for the H900 condition increases after all traps are filled, and that fitting of a higher diffusion coefficient is appropriate for late stages of charging (Figs. 1a, 1c, 1e). In the H900 condition, the higher trap concentration compared to the H1000 condition results in a steeper rise of the transient. Secondly, The late part of the decay transient is less steep for H900 compared to H1000, thus $D_{low\_20-10\%j_{ss}}$ is lower for the former. Thirdly, in the H900 condition, in the final part of the decay transient, a tail of residual current was observed until the current density dropped below 0.1 $\mu A/cm^2$ (Fig. 1d). All of these three observations indicate that the traps are slowly filled during the initial parts of the charging transient and are slowly emptied during the late parts of the decay transient. This conclusion is supported by the finding that the ratio between hydrogen emitted from reversible traps and the total hydrogen emitted during decay is higher for the H900 condition than for the SA and H1000 conditions, as shown in Table II. The diffusion coefficient decreases as the trap-

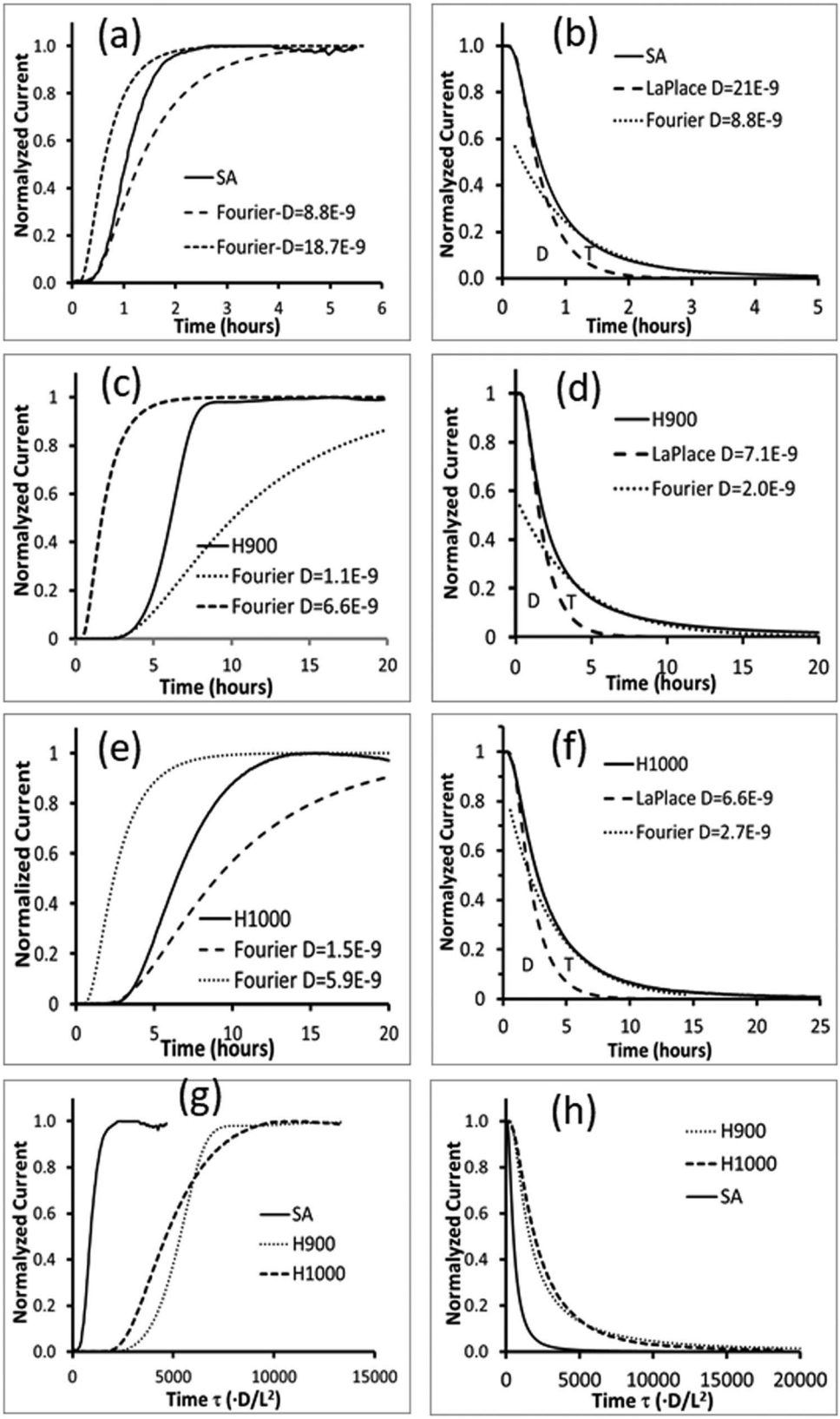

Figure 1. Electrochemical hydrogen permeation transients. The diffusion coefficients in this figure are in units of cm^2/s. Charging (a,c,e) and decay (b,d,f) normalized current densities (j/j_{ss}) versus time. (a,b) SA condition, membrane thickness $L = 172$ μm, steady-state current density $j_{ss} = 56.3$ μA/cm^2. (c,d) H900 condition, $L = 170$ μm, $j_{ss} = 49.5$ μA/cm^2. (e,f) H1000 condition, $L = 187$ μm, $j_{ss} = 11.4$ μA/cm^2. In the decay transients (b,d,f), the integral of the LaPlace fit of the 90% j_{ss} curve is the closest to the lattice diffusion data and is marked as D. The traps concentration is marked as T; it is the difference between the total desorbed hydrogen (the integral of the experimental curve) and the the integral of the LaPlace fit of the 90% j_{ss} curve. Fourier fit of the 20–10% J_{SS} curve is also presented. (g,h) Normalized current density vs. dimensionless time τ ($\tau = D_{Fe}t/L^2$, $D_{Fe} = 7.5 \times 10^{-5}$ cm^2/s[18]). The charging (g) and the decay (h) transients of the three specimen types.

Table II. Values of the diffusion coefficient D_{eff} ($\times 10^{-9}$ cm^2/s) at various stages of the charging and decay transients. Comparison is made to another precipitation hardened martensitic stainless steel, PH13-8Mo.

Steel	Transient type	Parameter	SA	H900	H1000
Custom 465	Charging	$D_{c\_10\% j_{ss}}$	10.0 ± 0.3	1.0±0.1	2.0±0.5
		$D_{c\_50\% j_{ss}}$	10.6 ± 0.6	1.4 ± 0.1	2.1 ± 0.3
		$D_{c\_63\% j_{ss}}$	11.1 ± 0.9	1.8 ± 0.1	2.4 ± 0.2
	Decay	$D_{d\_90\% j_{ss}}$	18.7 ± 2.3	6.6 ± 0.4	5.9 ± 0.3
		$D_{d\_50\% j_{ss}}$	15.2 ± 1.7	4.9 ± 0.5	4.6 ± .06
		$D_{d\_37\% j_{ss}}$	15.4 ± 1.8	4.7 ± 0.5	4.7 ± 0.2
		$D_{high\_90\% j_{ss}}$	18.7 ± 2.5	7.1 ± 0.5	6.1 ± 0.5
		$D_{low\_20-10\% j_{ss}}$	8.8 ± 1.1	1.8 ± 0.2	2.7 ± 0.1
		Traps (%)	22 ± 2	51 ± 0.5	28 ± 6
PH13-8Mo[8,9]	Charging	$D_{c\_63\% j_{ss}}$	56	24	22

ping sites are being emptied. Lower diffusion coefficients are fitted for the late stages of the decay transient than for the initial stages (Figs. 1d, 1f). Higher trap concentration is the reason for the lower slope of the decay transient for the H900 condition than for the H1000 condition.

Temperature programmed desorption (TPD).—Figure 3 shows the hydrogen TPD spectra of SA, H900 and H1000 specimens (after charging) at a heating rate of 20 °C/min. The spectra of the three types of specimens consist of a single hydrogen desorption peak, between room temperature and approximately 250°C. This peak reflects the interchange between the various traps during the desorption process; its position dependence on the heating rate allows determining the average activation energy of desorption and trap density.[19–21] It can be seen that both the peak area and peak temperature (i.e. the temperature at which maximum desorption rate is obtained) are higher for H900 compared to SA and H1000 specimens. The peak area in the case of H1000 is only slightly larger than that of SA. The peak area is proportional to the total concentration of desorbed hydrogen, the proportionality constant being the system calibration factor. For a quantitative analysis of hydrogen concentration, which is the ratio between the total amount of desorbed hydrogen and specimen mass, the TPD system was calibrated using a standard of TiH_2 (~4 wt% H) and the procedure described in Ref. 22. The calibration constant obtained from the calibration curve was calculated as 3.79×10^{-10} C/(μg-H). Using this value, the concentration of hydrogen was calculated; the values are summarized in the inset of Fig. 3. Each value of hydrogen concentration in this diagram is the average of four TPD measurements at different heating rates of 5, 10, 15, and 20 °C/min, as presented in Table III. It can be seen that the hydrogen concentration desrobed from the H900 specimen (60 ppm) is about 2.6 times higher than that from H1000 (23 ppm), and 3.75 times higher than that from SA (16 ppm) specimens. The repeatable high hydrogen concentration in H900 compared to SA and H1000 specimens, even when all samples were charged together with hydrogen, is an evidence for the relatively high concentration of hydrogen traps in the H900 age condition. A similar trend of a higher hydrogen concentration in the H900 condition of Custom 465 compared to the SA condition has been reported recently.[6]

Figure 4 presents a series of TPD spectra obtained at various heating rates (5–20 °C/min) for the SA (Fig. 4a), H900 (Fig. 4b) and H1000 (Fig. 4c) conditions. It can be seen that the peak temperature shifts to higher values with increasing heating rate, as expected. The observed shift of peak temperatures with heating rate can be used to determine the activation energies E_{aT} for hydrogen release from traps according to the Kissinger relation:[21,23]

$$\ln\left(\frac{\varphi}{T_p^2}\right) = \ln\left(\frac{AR}{E_{aT}}\right) - \frac{E_{aT}}{R}\cdot\frac{1}{T_p} \qquad [12]$$

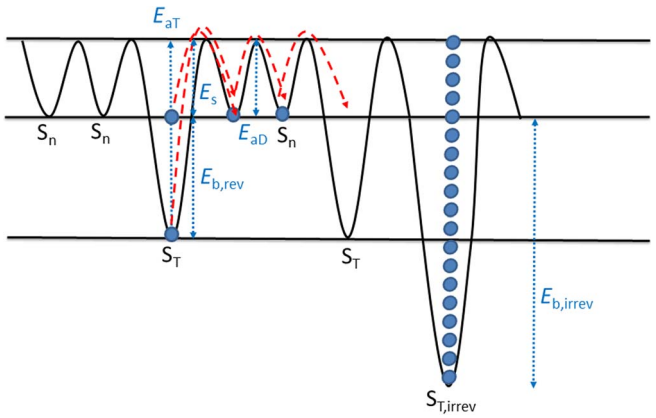

Figure 2. Energy levels of hydrogen around reversible and irreversible trapping sites. S_n is a normal interstitial site, S_T is a reversible trapping site, $S_{T,irrev}$ is an irreversible trapping site, E_{aD} is the activation energy of hydrogen lattice diffusion, E_{aT} is the activation energy for detrapping from a reversible trap, $E_{b,rev}$ is the reversible trap binding energy, $E_{b,irrev}$ is the irreversible trap binding energy, and E_s is the saddle point energy. Each blue circle represents a hydrogen atom. Our model assumes that all irreversible traps are full and that the reversible traps are refilled during the charging-decay cycles. Thus, diffusion is a combination of reversible trapping and lattice diffusion. The dash red arrows illustrate some possible hoping between interstitial and trap sites and the different activation energies involved.

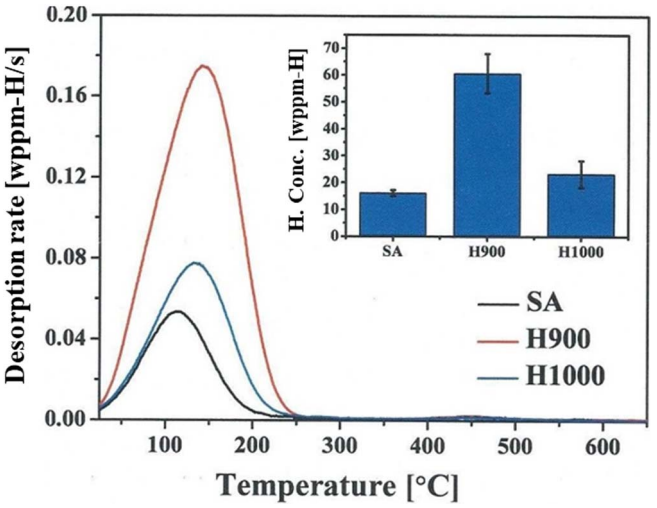

Figure 3. Comparison of the TPD spectra of all specimens for a heating rate of 20 °C/min.

Table III. Trapping parameters extracted from the TPD spectra of Custom 465: Hydrogen concentration and detrapping energies for the SA, H900 and H1000 conditions.

			hydrogen desorbed (ppm-H)			
	Heating rate (°K/min)	Temp. at desorption peak (°K)	Concentration	Average	R-square	E_{aT} (kJ/mol)
SA	5	363	16			
	10	374	16	16 ± 0.2	0.997	61 ± 5
	15	382.5	15.5			
	20	387	16			
H900	5	380.5	59			
	10	394	59	60 ± 2.7	0.980	44 ± 10
	15	407.5	58			
	20	416	64			
H1000	5	375.5	23			
	10	392	23	23.5 ± 1.7	0.990	49 ± 8
	15	402	22			
	20	407	26			

where T_p is the peak temperature (K), φ is the heating rate (K/s), A is the pre-exponential reaction rate constant (1/s), and R is the molar gas constant (8.31447 J/(mol·K)). The activation energy E_{aT} for hydrogen desorption or detrapping may be determined graphically by plotting $\ln(\frac{\varphi}{T_p^2})$ versus $\frac{1}{T_p}$ and calculating the slope of the line, as shown in Fig. 4d. The calculated activation energies are listed in Table III. It can be noticed that in SA condition E_{aT} is the highest (61 kJ/mol), in the H900 age condition is the lowest (44 kJ/mol), and in the H1000 age condition is slightly higher (49 kJ/mol), within the precision of measurements.

Discussion

The effect of the microstructure on the behavior of hydrogen in Custom 465 stainless steel was determined for three thermal

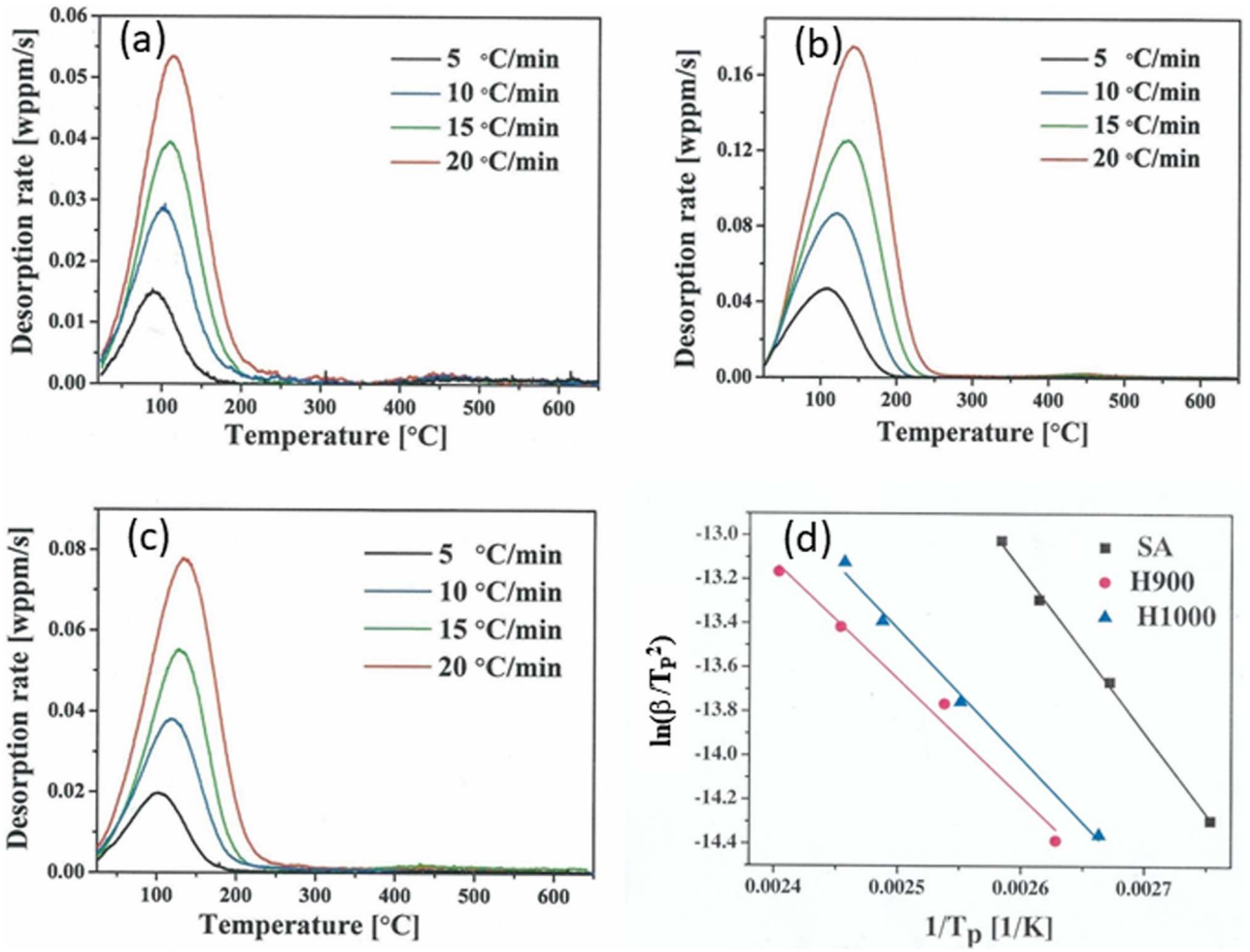

Figure 4. TPD spectra of charged specimens. Heating rates 5, 10, 15, and 20 °C/min. Solution annealed (a), H900 (b), H1000 (c) conditions. (d) The determination of the apparent activation energy according to the Kissinger relation.

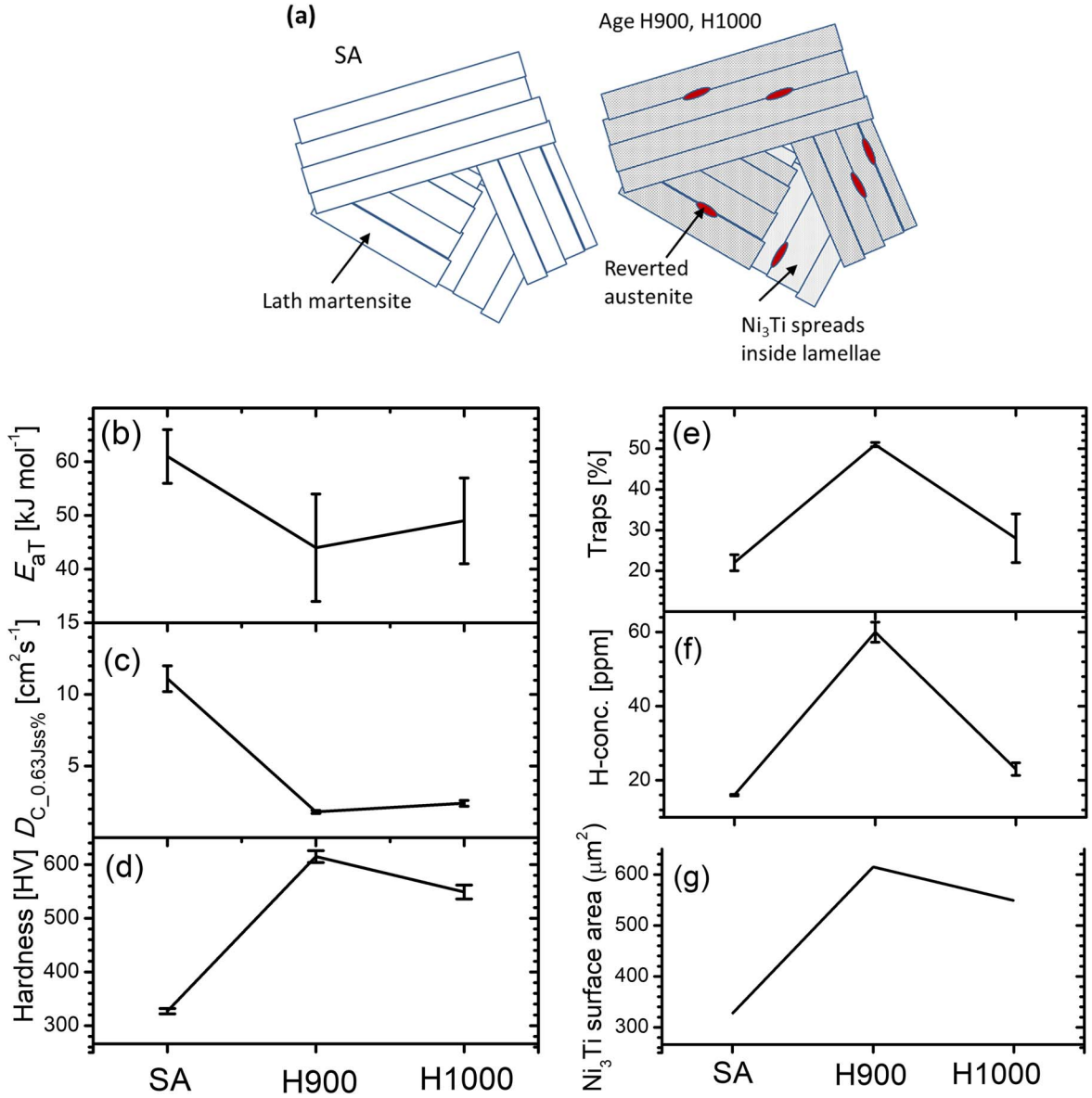

Figure 5. (a) Schematic illustration of the lath martensite structure, which consists of η-Ni_3Ti precipitates spreading inside the laths and nanoparticles of reverted austenite at inter-lath interfaces. The effect of thermal condition on the detrapping energy E_{aT} measured by TPD (b), the diffisivity measured by electrochemical permeation (c), the microhardness values[7] (d), the percentage of hydrogen released from traps out of the total amount of hydrogen decharged during the decay transient in the electrochemical permeation test (e), detrapped hydrogen concentration based on TPD (f), and the total surface area of the η-Ni_3Ti precipitates, as calculated from Eqs. 13 and 14 (g). These trends imply that the coherency of precipitates influences the trapping and diffusivity of hydrogen.

conditions. The microstructure in the SA condition consists of lath martensite, with η-Ni_3Ti precipitates spreading inside the laths and nanoparticles of reverted austenite at inter-lath interfaces,[4,7] as demonstrated schematically in Fig. 5a. In the H900 age condition, the peak of coherency of the η-Ni_3Ti precipitates is obtained, whereas H1000 is a slightly overage condition. The desorbed hydrogen concentration and average detrapping energy were deduced from TPD spectra, while the diffusion coefficient was determined based on electrochemical permeation tests. Complementing the results reported herein with the microstructural analysis reported in Ref. 7 and data analysis shown in Figs. 5b–5g, one can correlate the hydrogen behavior with the micro- and nano-structure of this steel.

The average detrapping energy measured in the SA condition is 61 kJ/mol. The lath interfaces and grain boundaries, as in the Fe-Ni lath martensitic microstructure, are considered in other alloys as high energy, irreversible trapping sites (>50 kJ/mol).[15,24–28] There are also reversible trapping sites with low energies (<50 kJ/mol) at lattice defects such as dislocations, vacancies, and "free" alloying elements with high affinity to hydrogen, in particular Ti. The value of 61 kJ/mol is similar to values reported in the literature for other lath martensitic steels. Novak et al.[27] reported a high average detrapping energy E_{aT} = 55 kJ/mol in AISI 4340 lath martensitic steel. Li et al.[29] determined E_{aT} = 61–62 kJ/mol for martensite interfaces, prior austenite grain boundaries, and mixed dislocation cores in an AERMET 100 lath martensite steel.

The measured average detrapping energies in the H900 and H1000 conditions are similar (44 and 49 kJ/mol, respectively), within the precision of measurement, and lower than the detrapping energy in the SA condition. We assume that the existence of reversible traps for hydrogen reduces the average detrapping energy in H900 and H1000, compared to the SA condition. In the H900 and H1000 age conditions, some of the "free" alloying elements that act as traps in the SA condition are bounded in the precipitates, e.g. the ≈1.5% Ti in the η-Ni_3Ti precipitates. It was reported that the low hydrogen-trap

binding energy of 11.4 to 11.6 kJ/mol in aged AERMET 100 can be associated with nanometer-scale, coherent M_2C (where M = 75 at.% Cr, 13 at.% Fe, or 12 at.% Mo) precipitates.[29] The activation energy for detrapping from nanosized TiC coherent precipitates in 0.42C–0.30Ti steel was reported to be in the range of 46–59 kJ/mol[28] at maximum hardness, depending on the tempering temperature prior to aging. Hence, it is suggested that the low energy traps in our case are also associated with η-Ni_3Ti precipitates, although the interfaces of the reverted austenite are also potential hydrogen traps.

The desorbed hydrogen concentration was determined by integrating the hydrogen desorption peaks in the TPD spectra. In the SA condition, the measured hydrogen concentration of 16 wtppm-H can be related to lattice traps (lattice defects and lath martensite interfaces). The hydrogen concentrations measured in the H900 and H1000 condition are 61 and 23 wtppm-H, respectively. Although the detrapping energies are similar, the concentration of desorbed hydrogen is about 2.6 times higher in the H900 than in the H1000 condition. The concentration of the desorbed hydrogen is much higher in the aged conditions than in the SA condition, consequently the average detrapping energy is lower. This is because in the SA condition there are mostly high-energy (irreversible) traps, while in the H900 and H1000 conditions there is also significant amount of hydrogen that is occupied in low-energy (reversible) traps, thus the average detrapping energy is lower. Those trends will be further explained later, considering the microstructural characteristics.

The diffusion coefficient in Custom 465 steel ($1–20\times10^{-9}$ cm^2/s) is significantly lower than in pure iron (7×10^{-5} cm^2/s[18]) even that they both have a BCC structure. This indicates that Custom 465 contains a higher concentration of traps. The diffusion coefficient is about 5 folds lower in the H900 and H1000 conditions than in the SA condition. The correlation between diffusivity, detrapping energies and hardness, as demonstrated in Fig. 5 for the different aging conditions, implies that the coherency of precipitates plays an important role. The existence of a minimal diffusion coefficient as a function of the coherency of Cr-carbide ($(Fe,Cr)_{23}C_6$) precipitation in the ferrite phase has been reported in other high-chromium steels, such as P91 (modified 9%Cr-1%Mo),[30] and in 12%Cr AISI 403 martensitic steel.[31] During the repetitive cycles of the electrochemical permeation tests, reversible traps and lattice diffusion play a major role in the diffusion process. The low concentration of reversible traps in the SA condition, as reflected by a higher average detrapping energy measured by TPD, is the reason for the high diffusion coefficient. Integrating the decay transients and comparing to the fitted curves reveal a higher percent of desorbed hydrogen for the H900 condition relative to the SA condition, and an intermediate value for the H1000 condition. This trend is similar to that of a higher hydrogen concentration in H900 compared to H1000 and SA, as observed by TPD.

The diffusivity of hydrogen in Custom 465 cannot be defined by a single value, since this steel is characterized by high traps concentration. The values of the diffusion coefficient are 2–3 times higher when the trap occupancy is high (i.e. during the final stages of the charging cycle and the initial stages of the decay, $D_{high\_90\%j_{ss}}$) than when the trap occupancy is low (i.e. during the initial stages of charging, $D_{c\_10\%j_{ss}}$, or the last stages of the decay transient, $D_{low\_20-10\%j_{ss}}$). This ratio between the values of the diffusion coefficient is similar for the three specimen types, thus implying that the main traps responsible to this phenomenon are the reversible traps in the martensite structure that are common to the three specimen types.

The minor differences in the charging and decay transients between the two age conditions, H900 and H1000, could stem from the (semi)coherency and size of the precipitates. The effect of reverted austenite can be neglected in both age conditions, as will be discussed below, and the martensite microstructure and lattice traps are similar as well, thus isolating the nano-precipitates as the dominant reason for the different hydrogen behavior. The diffusivity of hydrogen in this steel varies at different stages of the charging-decay cycles, according to the trap occupancy. In the H900 condition, the traps are slowly filled at the initial stages of the charging transient and are slowly emptied during the late stages of the decay transient. Due to the higher concentration of traps in the H900 compared to the other conditions, the trapping and detrapping processes are slower.

Assessing of detrapping sites in the microstructure.—Characterization of the traps in the microstructure is based on the correlation between the average detrapping energy E_{aT}, the diffisivity, the concentration of desorbed hydrogen, the total surface area of the η-Ni_3Ti precipitates and the hardness, as shown in Fig. 5, and the reverted austenite concentration as measured by XRD.[7] It is clear that the maximal hardness values are obtained at the peak of coherency, in H900, and that the hardness is slightly reduced as the precipitates become larger in H1000.[7]

The influence of the reverted austenite in the H900 and H1000 conditions on hydrogen behavior seems to be minor. First, the hydrogen concentration as determined by TPD is significantly lower in H1000 compared to H900, although the reverted austenite concentration increases. Second, the morphology of the austenite in both H900 and H1000 conditions seems as discrete nanosize patches at grain boundaries and lath interfaces, as analyzed by transmission Kikuchi diffraction in electron backscatter diffraction (TKD-EBSD).[7] In this microstructure, the barrier to hydrogen flow is low. In addition, the concentration of the reverted austenite is low, namely <5 vol.%, in these age conditions. Therefore, it seems that the effect of reverted austenite on hydrogen interaction in the H900 and H1000 conditions is low.

The influence of the precipitates on hydrogen interaction has been reported for (semi)coherent TiC,[28,32–35] V_3C_4[30,35–37] and (TiMo)C[19] precipitates in various tempered lath martensitic steels. It was proposed[15] that the TiC and V_3C_4 precipitates become more reversible trapping sites as their coherency is increased. It was argued that the large interface between the coherent TiC precipitates and the matrix was the main hydrogen trapping site, whereas the misfit dislocation cores on semicoherent V_3C_4 platelet precipitates were deep trapping sites.[34,35] Fig. 5 demonstrats the good correlation for all age conditions between desorbed hydrogen concentration, as measured by both TPD and electrochemical permeation tests, and the total surface area of the η-Ni_3Ti precipitates.

Calculation of the ratio between the surface area per volume of the η-Ni_3Ti precipitates in H900 and in H1000 was made according to Eqs. 13 and 14, in order to explain the difference in the desorbed hydrogen concentration and to support the assumption that the precipitate's interface is the major trapping site:

$$V_{Ni_3Ti} = n_{900} \cdot v_{900} = n_{1000} \cdot v_{1000} \quad [13]$$

where V_{Ni_3Ti} is the total volume fraction of the η-Ni_3Ti precipitates, which is assumed to be the same in both age conditions, v_{900} and v_{1000} are the calculated volumes of the rod-shaped precipitates for the H900 (diameter 2.8 ± 0.4 nm, length 7.0 ± 1.0 nm) and H1000 (diameter 7.6 ± 1.0 nm, length 31.7 ± 7.0 nm) conditions, respectively, and n_{900} and n_{1000} are the numbers of precipitates per volume fraction in both conditions.

$$\frac{S_{900}}{S_{1000}} = \frac{n_{900} \cdot s_{900}}{n_{1000} \cdot s_{1000}} \quad [14]$$

where s_{900} and s_{1000} are the surface areas of a single rod-shaped precipitate in the H900 and H1000 conditions, respectively, and S_{900} and S_{1000} are the total surface areas of precipitates in both conditions.

The calculation of the concentration of precipitates in Eq. 13 is based on the assumption that the volume fraction of the η-Ni_3Ti precipitates in both conditions is similar, based on thermodynamic calculation of the expected equilibrium volume fraction of the η-Ni_3Ti phase presented in our previous work.[7] According to Eq. 13, the number of precipitates per volume fraction is 32 times higher for H900 than for H1000. The total surface area of precipitates, as calculated according to Eq. 14, is 2.9 times higher in the H900 condition than in the H1000 condition. This is in accordance with the measurement of 2.6 times higher hydrogen desorption from the H900 material than from the H1000 material.

Conclusions

Hydrogen behavior in Custom 465 precipitation hardened martensitic stainless steel was studied. The diffusivity, solubility and average detrapping energies were determined by electrochemical permeation (EP) and thermal programmed desorption (TPD) experiments, comparing the peak age H900 condition, in which the η-Ni_3Ti precipitates are (semi)coherent, to the slightly overage H1000 condition and to the solution annealed (SA) condition. A high concentration of reversible (low energy) trapped hydrogen was found in the H900 condition, which lowers both the diffusivity and the average detrapping energy compared to the SA condition. The diffusion coefficient of hydrogen in the steel varies in different stages of the charging-decay cycles, according to the trap occupancy. This phenomenon emphasizes that trapping is a dominant phenomenon in this steel, as reflected by the low hydrogen diffusivity relative to pure iron. Semicoherent η-Ni_3Ti precipitates have significant effect on hydrogen behavior; their high surface area and the stress field around them are two possible factors. The reverted austenite seems to have only a minor effect on hydrogen interaction with this steel.

Acknowledgments

This work was supported by grant No. 205–13 from the Pazi Foundation of the Israeli Council of Higher Education and the Israel Atomic Energy Commission. We thank Shlomo Levi and Yair Goerge for their technical assistance.

ORCID

N. Eliaz https://orcid.org/0000-0002-1184-4706

References

1. Custom 465 stainless steel, Technical datasheet, Carpenter Company, 2014.
2. C. S. Carter, D. G. Farwick, A. M. Ross, and J. M. Uchida, "Stress corrosion properties of high-strength precipitation hardening stainless steels," *Corros*, **27**, 190 (1971).
3. D. E. Wert and T. N. Werley, "Comparison of stress corrosion cracking and hydrogen embrittlement resistance of high strength aerospace alloys," *In 2010 TMS Annual Meeting and Exhibition - Supplemental Proceedings*, **3**, 673 (2010).
4. S. Ifergane, E. Sabatani, B. Carmeli, Z. Barkay, V. Ezersky, O. Beeri, and N. Eliaz, "Hydrogen diffusivity measurement and microstructural characterization of Custom 465 stainless steel," *Electrochim. Acta*, **178**, 494 (2015).
5. Y. Lee and R. P. Gangloff, "Measurement and modeling of hydrogen environment-assisted cracking of ultra-high-strength steel," *Metall. Mater. Trans. A*, **38**, 2174 (2007).
6. G. L. Pioszak and R. P. Gangloff, "Hydrogen environment assisted cracking of a modern ultra-high strength martensitic stainless steel," *Corros*, **73**, 1132 (2017).
7. S. Ifergane, M. Pinkas, Z. Barkay, E. Brosh, V. Ezersky, O. Beeri, and N. Eliaz, "The relation between aging temperature, microstructure evolution and hardening of Custom 465 stainless steel," *Mat. Charac.*, **127**, 129 (2017).
8. L. W. Tsay, M. Y. Chi, H. R. Chen, and C. Chen, "Investigation of hydrogen sulfide stress corrosion cracking of PH 13-8-Mo stainless steel," *Mater. Sci. Eng. A*, **416A**, 155 (2006).
9. L. W. Tsay, M. Y. Chi, Y. F. Wu, J. K. Wu, and D. Y. Lin, "Hydrogen embrittlement susceptibility and permeability of two ultra-high strength steels," *Corros. Sci.*, **48**, 1926 (2006).
10. M. A. V. Devanathan and Z. Stachurski, "The adsorption and diffusion of electrolytic hydrogen in palladium," *Proc. R. Soc. London*, **A270**, 90 (1962).
11. ASTM G148-97, Standard practice for evaluation of hydrogen uptake, permeation, and transport in metals by an electrochemical technique. *ASTM International:*, 2003.
12. BS EN ISO 17081:2014E: *Method of measurement of hydrogen permeation and determination of hydrogen uptake and transport in metals by an electrochemical technique.* ISO. 2014.
13. A. Turnbull, *Standardization of hydrogen permeation test*, in in A. Turnbull, (Ed.), Hydrogen Transport and Cracking in Metals. UK (1994) 129.
14. A. Danon, I. Avraham, and J. Koresh, "Temperature programmed desorption-mass spectrometer with supersonic molecular beam inlet system," *Rev. Sci. Inst.*, **68**(12), 4359 (1997).
15. G. M. Pressouyre, "A classification of hydrogen traps in steel," *Metall. Trans. A*, **10**, 1571 (1979).
16. A. McNabb and P. K. Foster, "A new analysis of the diffusion of hydrogen in iron and ferritic steels," *Trans. Metall. Soc. AIME*, **227**, 618 (1963).
17. R. A. Oriani, "The diffusion and trapping of hydrogen in steel," *Acta Metall*, **18**, 147 (1970).
18. T. Zakroczymski, "Adaptation of the electrochemical permeation technique for studying entry, transport and trapping of hydrogen in metals," *Electrochim. Acta*, **51**, 2261 (2006).
19. A. Nagao, M. L. Martin, M. Dadfarnia, P. Sofronis, and I. M. Robertson, "The effect of nanosized (Ti,Mo)C precipitates on hydrogen embrittlement of tempered lath martensitic steel," *Acta Mater*, **74**, 244 (2014).
20. K. Takai, H. Shoda, H. Suzuki, and M. Nagumo, "Lattice defects dominating hydrogen-related failure of metals," *Acta Mater*, **56**, 5158 (2008).
21. N. Eliaz, D. Eliezer, E. Abramov, D. Zander, and U. Köster, "Hydrogen evolution from Zr-based amorphous and quasicrystalline alloys," *J. Alloys Compd*, **305**(1–2), 272 (2000).
22. F. von Zeppelin, M. Haluška, and M. Hirscher, "Thermal desorption spectroscopy as a quantitative tool to determine the hydrogen content in solids," *Thermochi. Acta*, **404**, 251 (2003).
23. H. E. Kissinger, "Reaction kinetics in differential thermal analysis," *Anal. Chem.*, **29**, 1702 (1957).
24. G. M. Pressouyre and I. M. Bernstein, "A quantitative analysis of hydrogen trapping," *Metall. Trans.*, **A9**, 1571 (1978).
25. I. M. Bernstein, "The effect of hydrogen on the deformation of iron," *Scr. Metall.*, **8**(4), 343 (1974).
26. J. P. Hirth and J. R. Rice, "On the thermodynamics of adsorption at interfaces as it influences decohesion," *Metall. Trans.*, **A11**(9), 1501 (1980).
27. P. Novak, R. Yuan, B. P. Somerday, P. Sofronis, and R. O. Ritchie, "A statistical, physical-based, micro-mechanical model of hydrogen-induced intergranular fracture in steel," *J. Mech. Phys. Solids*, **58**, 206 (2010).
28. F. G. Wei, T. Hara, and K. Tsuzaki, "Precise determination of the activation energy for desorption of hydrogen in two Ti-added steels by a single Thermal-Desorption Spectrum," *Metall. Mater. Trans.*, **B35**, 587 (2004).
29. D. Li, R. P. Gangloff, and J. R. Scully, "Hydrogen trap states in ultrahigh-strength AERMET 100 steel," *Metall. Mater. Trans.*, **A35**(3), 849 (2004).
30. C. H. Noreña and P. Bruzzoni, "Effect of microstructure on hydrogen diffusion and trapping in a modified 9%Cr–1%Mo steel," *Mater. Sci. Eng.*, **A527**, 410 (2010).
31. Y. Sakamoto and U. Hanada, "Effect of heat treated structure on diffusion of hydrogen in martensitic type 403 stainless steel," *Trans. JIM*, **18**, 466 (1977).
32. A. Asaoka, G. Lapasset, M. Aucouturier, and P. Lacombe, "Observation of hydrogen trapping in Fe-0.15 wt% Ti alloy by high resolution autoradiography," *Corros*, **34**(2), 39 (1978).
33. F. G. Wei and K. Tsuzaki, "Quantitative analysis on hydrogen trapping of TiC particles in steel," *Metall. Mater. Trans.*, **A37**, 331 (2006).
34. J. Takahashi, K. Kawakami, Y. Kobayashi, and T. Tarui, "The first direct observation of hydrogen trapping sites in TiC precipitation-hardening steel through atom probe tomography," *Scr. Mater.*, **63**, 261 (2010).
35. J. Lee, T. Lee, Y. J. Kwon, D. J. Mun, J. Y. Yoo, and C. S. Lee, "Role of Mo/V carbides in hydrogen embrittlement of tempered martensitic steel," *Corros. Rev.*, **33**(6), 433 (2015).
36. S. Yamasaki, M. Kubota, and T. Tarui, "Evaluation methods for delayed fracture susceptibility of steels and development of high tensile strength steels with high delayed fracture resistance," *Nipon Steel Technical Report*, **80**, 50 (1999).
37. J. Takahashi, K. Kawakamia, and T. Taruib, "Direct observation of hydrogen-trapping sites in vanadium carbide precipitation steel by atom probe tomography," *Scr. Mater.*, **67**, 213 (2012).